This is a post-print version of
Railway embankment failure due to ballast layer breach caused by inundation flows
by
Ryota Tsubaki, Yoshihisa Kawahara and Yasuhiro Ueda
submitted and accepted in
Natural Hazards
The final publication is available at link.springer.com
http://link.springer.com/article/10.1007/s11069-017-2789-3

Railway embankment failure due to ballast layer breach caused by inundation flows

RYOTA TSUBAKI[a*], YOSHIHISA KAWAHARA[b] and YASUHIRO UEDA[c]

[a] Associate Professor, Department of Civil Engineering, Nagoya University, Furo-cho, Chikusa-ku, Nagoya 464-8603 Japan
(Tel: 81-52-789-4625, e-mail: rtsubaki@civil.hiroshima-u.ac.jp)
[b] Professor, Department of Civil and Environmental Engineering, Hiroshima University
(Tel: 81-82-424-7821, Fax: 81-82-424-7821, e-mail: kawahr@hiroshima-u.ac.jp)
[c] Tokyo Metropolitan Government

* Corresponding author.

Abstract

A railway embankment constructed on a floodplain is at risk of damage due to flooding flows. The process and critical conditions that lead to railway embankment damage during flooding are not clearly understood, rendering risk estimations impossible and hindering the development of flood-resilient rail systems. For this work, we first reviewed records of railway damage in flood plains and flows through the ballast layer. The breaching process was selected as the focus of our study. We secondly specified the fundamental characteristics of flows through a ballast layer. The critical flow rate per unit width and the minimum upstream water depth required for initiating extensive ballast breaching were experimentally evaluated using a full-scale ballast layer with rails and sleepers constructed using materials originally utilized in actual railways. A two-dimensional flow model was then employed for estimating the flow

through a ballast layer that was placed on an impermeable base embankment. A simple ballast breaching model was also employed in order to explore a higher flow rate condition that could not be represented in our experiment due to limited facilities. The breaching pattern represented by the simulation model corresponded to the breaching pattern observed in the experiment. In addition to the above, here, we also discuss the ballast breaching process based on qualitative field records and quantitative experimental results, as well as the ballast breaching process as represented by the simulation.

Keywords: embankment breaching, railway embankment, ballast, non-Darcian flow, shallow water flow model

1. Introduction

1.1 Inundation disasters and embankments on floodplains

Infrastructures, such as embankments for transportation, located near rivers have been damaged during extreme inundation events (refer to Figure 1, Tsubaki et al. 2011, Polemio and Lollino 2011). In mountainous regions, most railway and road embankments are constructed parallel to river courses. The rapid and intense runoff of small mountainous catchments may cause sudden inundation during intense rain events; and rapid inundation flow accompanied by sediment transport can affect the shape of the land and damage infrastructure within the floodplain. A number of flood records have demonstrated that railway embankments are damaged due to flooding flows (Tsubaki et al. 2012, Fujita et al. 2012). Damage in one section of a railway network impacts the entire operation of the railway system and the railway service becomes highly restricted until the railway network is fully recovered. Therefore, estimating and reducing failure risk for railway embankments is essential for achieving high availability for transportation in pluvious regions.

Embankments for transportation serve the secondary functions of suspending the expansion of inundation flows and changing the flood flow direction. Following the 2011 Tohoku earthquake and tsunami disaster, transportation embankments were adopted as one of the primary mitigation measures for inundation risks in Japan's tsunami recovery plan. Even so, transportation embankments adopted as a flood barrier have the potential to be breached, as same as regular river embankments, if the hazard level is more intense than expected when designing each embankment. If these transportation embankments are damaged by flooding flows, the expected function of inundation flow control significantly changes. For a case such as this, transportation embankments pose the potential for expanding the area of damage surrounding a breached embankment.

Critical flow conditions and the process of railway embankment breaching are not well understood. However, evaluating the critical condition of a railway embankment breach is essential for designing, constructing, and maintaining railway systems and services. Understanding the process of railway embankment breaching is also critical for adopting measures that can render embankments more resilient to breaching damage.

1.2 The structure of railway embankments

A single-track railway embankment is a typical example of a railway in rural, and in many cases flood-prone, areas. As shown in Figure 2, this type of railway embankment consists of the following features from top to bottom: (a) a pair of rails, (b) railway sleepers, (c) a ballast layer, and (d) a base embankment. Both the base embankment and the ballast layer consist of earthen materials. Therefore, seepage flows occur in these earthen components during rainfall and inundation.

The materials utilized for base embankments are selected based on economic considerations, stability against loading, and the drainage performance of rain water; soil materials are generally diverted from a neighboring cut earth site (e.g., Railway Technical Research Institute 2007). The material employed for the ballast is prepared according to railway construction standards, but the tolerance of the base embankment soil to overtopping flows is not explicitly considered (Railway Technical Research Institute, 2007).

Rails and sleepers (the upper structure) are closely connected to one another and supported by the ballast layer. The upper structure frequently remains after the supporting ballast layer and, in the past, base embankments have been almost completely washed away by flooding flows (e.g., Figure 1). The ballast in an operating railway is often gradually compacted and fractured by periodic loading generated by the passage of railcars. If rails are displaced beyond the accepted range from original locations, the positions of the rails are corrected by rearranging the ballast layer. Overly fractured ballast material exhibits low shock-absorbing performance and is subsequently replaced with new material.

1.3 The failure mode of embankments

Major causes of earthen embankment failures, including the failures of dams, levees, and barriers are (a) overtopping, (b) structural defects, and (c) piping (ASCE/EWRI Task Committee 2011). For earthen dam failures, these three causes equally contribute to the overall failure rate (Costa 1985), but this may not be the case for railway embankment failures. In guidelines published by India's Ministry of Railways (2005), breach/washout damage to railway embankments is categorized based on the cause of damage from: (a) continuous rains, (b) floods

and receding water, (c) vertical sag (bad bank), (d) inadequate openings, or (e) scouring damage. Type of damage is also categorized into five varieties by India's Ministry of Railways (2005).

Figure 3 displays fractions for the occurrence of natural hazards causing failures along railways from 1999 to 2010 in Japan. The most frequent type of failure was a fallen tree due to wind; damage that is comparatively easy in regards to recovery. Other types of failures involved severe damage caused by rainfall and water flow (the dark gray bars in Figure 3 correspond to damage caused by water flow). Embankment erosion and ballast breach, the main topics of this paper, represented 15% of the total damage rate. Note that the embankment erosion presented here contains slope breaching due to overtopping flows (Figures 4a and b) in addition to erosion due to neighboring rivers and slope failures due to rain infiltration.

The heights of railway embankments are generally small as compared to dams and river banks. Thus, water pressure acting on railway embankments during flooding is relatively small and the duration of the water pressure acting on such embankments is comparatively short. For a case where deep flood water impoundment occurs for a substantial period of time, embankment seepage failure (see Figure 4c) occurs. The embankment failure of the Acquaviva railway in southern Italy during 2005 is an example of seepage failure. The Acquaviva railway embankment, with a height of 7 meters, collapsed due to the 6 meter depth of the upstream impoundment and a 6 hour seepage flow (Polemio and Lollino 2011). The embankment core of the Acquaviva railway consisted of coarse material, and the estimated permeability coefficient was large. Both factors caused rapid seepage failure following a short inundation duration (Polemio and Lollino 2011).

For a comparatively small-scale railway embankment (with a height of a few meters), the majority of water-flow-related failures are assumed to be caused by the overtopping of inundation water. Such an assumption is supported by a number of records of railway damage due to floods (e.g., Kaneko 2010). In particular, evidence of ballast breaching, occasionally accompanied by lee slope breaching during severe flood cases, has been widely observed in terms of flooded railways (Kaneko 2010), and many severe railway embankment breaches seem to be initiated by ballast breaches (Figure 4b) and then followed by base embankment erosion (Figure 4a; Tsubaki et al. 2012).

1.4 Objective of this study

For this study, we investigated the process and critical conditions of railway embankment failure initiated by ballast seepage. The characteristics of flows through a ballast layer with/without upper structures were first investigated, and the critical flow rate per unit width as well as the minimum upstream water depth required to initiate extensive ballast breaching were experimentally evaluated. A two-dimensional flow model was then employed in order to

135 determine the process of ballast layer breaching occurring under higher flow rate conditions that
136 could not be represented in our experiment due to limited facilities. Here, we summarize
137 experimental and numerical results that can be utilized in the future for estimating the failure
138 risk of railways and embankments in flood plains.
139
140 **2. Experiment**
141 Seepage flow through a ballast layer occurs when there is a differential in the hydraulic head
142 across an embankment that is caused by flood water impounding an embankment. If the
143 upstream impounded water level and the corresponding flow rate exceed critical values,
144 breaching of the ballast layer will commence.
145 In this section, we evaluate the material properties of both new and used ballasts. A channel
146 experiment that simulates seepage flow through a railway ballast layer was conducted in order
147 to understand the critical flow condition that causes ballast layer breaching. The properties and
148 conditions evaluated in this section are employed in the numerical simulation provided in the
149 next section so we can discuss railway embankment breaching that occurs on larger spatial
150 scales and under higher flow conditions that were beyond the scope of our original experiment.
151
152 ***2.1 Ballast material***
153 The properties of two types of ballast materials were investigated. The first material
154 consisted of a new ballast that was directly shipped from a supplier. The second material
155 consisted of a used material that was removed from an operating railway after approximately
156 five years. The new ballast material was the main type of material used in our experiment, but
157 we also specified the properties of the used material because ballast material in an operating
158 railway is expected to have properties in a range between those of the new and used materials.
159 The grain size distribution, density, and porosity of the materials are provided in Figure 5 and
160 Table 1. The used material contained a larger number of small-diameter particles and its
161 porosity was smaller than the porosity of the new material. The source of each gravel to be
162 sampled differed (Hiroshima prefecture for the new material and Hyogo prefecture for the used
163 material), creating a small difference in the corresponding densities. Weathering may have also
164 affected the density difference.
165
166 ***2.2 Parameterization of energy loss model for seepage flow through the ballast material***
167 Flow through a ballast layer experiences a decrease in total flow energy due to skin friction
168 and turbulence within the pore space in the case of a large pressure gradient (Hassanizadeh and
169 Gray 1987, Trussell and Chang 1999) such as that found under an overtopping flow condition.

This type of energy loss model is referred to as the non-Darcian model or the Forchheimer model. The energy slope, I_e, for a non-Darcian porous flow is represented as:

$$I_e = U(a + bU) \tag{1}$$

where U is the bulk velocity, a is a parameter representing energy loss related to viscosity and skin friction, and b is a parameter related to turbulent energy loss (for detailed derivations, refer to, for example, Masuoka and Takatsu 1996). The model with $b = 0$ is referred to as the Darcian flow model. The parameters a and b have physical underpinnings (Ward 1964, Michioku et al. 2005) and there are various semi-empirical models that can be used to determine these parameters (e.g., Arbhabhirama and Dinoy 1973, Shimizu 1992). Since the representative particle diameter and the porosity, as well as the grain size distribution, the shape of each particle, the roughness of gravel surfaces, etc., also affect flow and energy loss within the pore space and since a universal model that considers all of the above-mentioned effects has not been established, in practice, the empirical calibration is a valid and feasible method for determining parameters a and b.

To evaluate energy loss, flow through a small ballast layer with a base length of 0.75 m and a height of 0.25 m, as shown in Figure 6, was investigated. The flow rate per unit width supplied from the upstream varied from 0.0015 to 0.018 m^2/s. The flow rate per unit width, q (m^2/s), is used instead of the total flow rate, Q (m^3/s), because the total flow rate is proportionally changed in relation to the longitudinal (span-wise) length of the focused embankment. Water depth at the upstream section (h_{in} defined in Figure 6) varied from 0.110 to 0.265 m as a result of the flow rate increase. The water surface profile of flow through the ballast layer (between points h_{in} and h_{out} shown in Figure 6) is represented based on Eqn. 1. The observed h_{out} and the flow rate, q, are used with Eqn. 1 to calculate the water surface profile, h_{in}, that is subsequently calculated using a one-dimensional Bernoulli equation (Michioku et al. 2005). Values for parameters a and b that minimized error between the calculated h_{in} and the observed h_{in} were computed.

The non-Darcian energy loss models that best represent our experimental results are:

$$I_e = U(0.79 + 25.1U) \tag{2}$$

for the new ballast and

$$I_e = U(5.00 + 1.20U) \tag{3}$$

for the used ballast.

Figure 7 compares the calculated upstream water depth evaluated using Eqns. 2 and 3 with the measured upstream water depth. The evaluated and measured values, as shown by the filled circles, agreed. This agreement indicates that Eqns. 2 and 3 accurately represent energy loss for ballast seepage flow from small to large flow conditions. In Figure 7, the upstream water depth, evaluated using grain size and porosity, is also plotted with the cross mark. The parameters a and b in Eqn. 1 were evaluated based on (Arbhabhirama and Dinoy 1973):

$$a = \frac{\nu}{gK}, \tag{4}$$

$$b = 100\left(\frac{d_m}{\sqrt{K/\phi}}\right)^{-3/2} \cdot \frac{1}{g\sqrt{K}} \tag{5}$$

where ν is the kinetic viscosity, g is the gravitational acceleration, ϕ is the porosity, and K is the length scale; and is evaluated based on:

$$K = (0.0139\, d_m)^2 \tag{6}$$

as used in Shimizu (1992) where d_m is the representative diameter of the particles. Using Eqns. 4 to 6, we obtained $a = 0.516$ and $b = 66.2$ for the new ballast and $a = 0.781$ and $b = 85.6$ for the used ballast. The estimated water depth (shown by the crosses in Figure 7) show respectable agreement with the measured value especially for the used material. However, our empirical models (plotted using filled circles) displayed better agreement with the measured water depth. The length scale estimated using Eqn. 6 does not consider differences in grain size distributions, the shape of each grain, or the roughness of gravel surfaces and may limit the accuracy of the energy loss estimation. Ballast material, especially the ballast that was not used, has a distinct angular shape as compared to usual sediment grains and may cause underestimation of the pore scale and an overestimation of energy loss and upstream water depth.

2.3 The ballast breaching experiment

An experimental flume with a width of 1 m and a length of 5.5 m was constructed for full-scale ballast experiments (refer to Figure 8 for a sectional view of the flume). Full-scale embankments with and without sleepers and rails were installed in a cross-sectional direction within the flume. The new ballast material was used to build the embankments. Water was supplied from the upstream end (x = -5.5 m in Figure 8) and was then impounded in the upstream section enclosed by the channel walls and the ballast layer. Seepage water flowed through the ballast layer (-4.3 m < x < 0 m). The downstream end of the channel (x = 0 m in Figure 8) was opened and was connected to a drainage channel in order to simulate the water drop in a downstream slope that occurs in an actual rail embankment.

Rails and sleepers (upper structure) were arranged in three configurations (Figure 9) in order to evaluate the effect of the upper structure on the breaching process, the critical condition that begins ballast layer breaching. Case A consisted of a ballast layer without sleepers or rails. Case B consisted of a ballast layer with two rails and one sleeper located at the center of the channel. Case C consisted of an embankment with rails and two sleepers. In Case C, two sleepers were placed on both sides of the channel.

Water was supplied to the upstream reservoir at a small flow rate. The water stage at points x = -1.12 m, -2.42 m, and -4.34 m (as defined in Figure 8) was measured using scales installed inside the channel. The submerged water level was observed through a Plexiglas side wall at points x = -1.12 m and -2.42 m, whereas the open-water level was observed from the inside of the channel at point x = -4.34 m. The flow rate was increased in a stepwise manner once the water surface profile stabilized (refer to Figures 10a and b for the downstream flow situation for the initial and intermediate phases, respectively). The flow rate was increased until maximum pump capacity (q = 0.048 m^2/s) was attained. The flow rate supplied at the time corresponding to the beginning of an extensive slope collapse was recorded (as denoted by the solid lines in Figure 11b). Figure 10c displays the breached ballast layer following flow at the maximum flow rate.

The width of the breached area yielded a variation from 0.5 to 0.8 m (refer to Figure 10c for a result for Case B). The results are inconclusive with regard to whether the observed breaching width was affected by the channel width (B = 1.0 m). However, the distance between the sleepers (0.52 m in the two sleeper experiments and 0.45 m in the 2009 Hyogo damaged section shown in Figure 1a) may be one of the regulating factors of the spatial heterogeneity of ballast breaching.

Figure 11 provides the relationship between flow rate and water depth. Water depths for the three cases at point x = -1.12 m for the embankment (0.52 m upstream from the downstream end of the embankment) were almost identical, regardless of differences within the upper structure. At the downstream end of the embankment, a control section is formed and the water surface profile is determined from the downstream direction to the upstream direction (Michioku et al. 2005). As a result, the difference in the upper structure of the embankment did not impact the relationship between the downstream water depth and the flow rate.

The upstream water depth (Figure 11b, at x = -4.34 m) followed a different trend based on the arrangement of the upper structure. If the water level was less than the elevation of the sleeper bottom, the relationship between the water stage and the flow rate was identical. For a situation in which water depth in the upstream area exceeded 0.5 m, the upstream water depth was dependent upon differences in the upper structure. The upper structure reduced the cross-sectional area through which water could flow, which increased the upstream water depth

for Cases B and C. The critical water depths at the onset of continuous ballast breaching (as shown in Figure 10b) were 0.55, 0.67, and 0.68 m for Cases A, B, and C, respectively. The height of the ballast layer was 0.5 m, so the critical water level for the three cases surpassed the level of the ballast top. Critical flow rates per unit width for this extensive breaching were 0.04, 0.046, and 0.044 m^2/s for Cases A, B, and C, respectively. The critical flow rate and the upstream water depth required to begin breaching in Cases B and C were almost identical.

3. Analysis of the embankment breaching process using a numerical model

In the previous section, the properties of seepage flow through the ballast layer and the embankment breaching process were physically evaluated. However, due to limited experimental facilities, our evaluation was limited during the initial phase of breaching. In this section, a two-dimensional flow model coupled with the seepage flow and ballast breaching models is used to comprehensively investigate the process of railway embankment breaching initiated from ballast breaching. Although the model was developed based on a previous flow model (Tsubaki et al. 2008; Tsubaki and Fujita 2010), porosity and energy loss through the ballast area were considered (e.g., Guinot and Soares-Frazão 2006, Sanders et al. 2008) and a new ballast breaching model was also introduced.

Due to the limitations arising from the model framework, the overtopping flow of the ballast layer and the effect of the upper structure of the ballast layer were neglected in the model. These model limitations reduced accuracy for the upstream water level prediction but did not directly impact the breaching process occurring at the downstream end of the embankment because water flow through the ballast layer was subcritical flow, so the flow profile was determined from the downstream to the upstream.

Below, based on the new ballast reported in the previous section, the calculated water profile in the ballast section is compared to results obtained for the embankment breach experiment. The sensitivity of the grid size and model parameters to the calculated results are evaluated. The process of the breached area expansion and impacts on the upstream water stage are analyzed. We finally discuss what will occur after ballast breach penetration. The two-dimensional flow model used here has limited ability for representing all of the three-dimensional features of seepage flow within the ballast layer. Therefore, discussion in this section focuses on a phenomenological breaching process.

3.1 The flow model

The following two-dimensional, shallow-water equations were employed (Guinot and Soares-Frazão 2006, Soares-Frazão et al. 2008, Sanders et al. 2008):

306 $$\frac{\partial \phi h}{\partial t}+\frac{\partial \phi hu}{\partial x}+\frac{\partial \phi hv}{\partial y}=0, \tag{7}$$

307 $$\frac{\partial \phi uh}{\partial t}+\frac{\partial \phi u^2 h}{\partial x}+\frac{\partial \phi uvh}{\partial y}+\frac{g}{2}\frac{\partial \phi h^2}{\partial x}-gh\frac{\tau_{sx}-\tau_{bx}-\tau_{px}}{\rho}=0, \tag{8}$$

308 $$\frac{\partial \phi vh}{\partial t}+\frac{\partial \phi uvh}{\partial x}+\frac{\partial \phi v^2 h}{\partial y}+\frac{g}{2}\frac{\partial \phi h^2}{\partial y}-gh\frac{\tau_{sy}-\tau_{by}-\tau_{py}}{\rho}=0 \tag{9}$$

309

310 where h is the depth of the flow; u and v are the depth-averaged water flow velocity components
311 in the x direction and y direction, respectively; t is the time; τ_{bx} and τ_{by} are related to the bed
312 slopes in the x and y direction, respectively; ρ is the mass density of water; and τ_{sx} and τ_{sy} are the
313 bed shear stresses, defined as:

314 $$\frac{\tau_{bx}}{\rho}=-g\phi h\frac{\partial z_b}{\partial x}+g\frac{h}{2}\frac{\partial \phi}{\partial x},\frac{\tau_{by}}{\rho}=-g\phi h\frac{\partial z_b}{\partial y}+g\frac{h}{2}\frac{\partial \phi}{\partial y}, \tag{10}$$

315 $$\frac{\tau_{sx}}{\rho}=\phi\frac{n^2 u\sqrt{u^2+v^2}}{h^{4/3}},\frac{\tau_{sy}}{\rho}=\phi\frac{n^2 v\sqrt{u^2+v^2}}{h^{4/3}} \tag{11}$$

316 where n is Manning's roughness coefficient and z_b is the local bed elevation. Head loss within
317 the porous area ($0\le\phi<1$) was evaluated using the non-Darcian resistance model:

318 $$\frac{\tau_{px}}{\rho}=-g\phi h\frac{\partial H_l}{\partial x}=-gh\phi^2 u\left(a+b\phi\sqrt{u^2+v^2}\right),\frac{\tau_{py}}{\rho}=-g\phi h\frac{\partial H_l}{\partial y}=-gh\phi^2 v\left(a+b\phi\sqrt{u^2+v^2}\right) \tag{12}$$

319 where a and b are coefficients based on the properties of a porous medium and where values
320 empirically determined in the previous section were used.

321 The finite volume method (FVM) combined with a shock-capturing scheme in an
322 unstructured triangulate grid system was employed in order to discretize the fundamental
323 equations (Shige-eda et al. 2002, Shige-eda and Akiyama 2003, Soares-Frazão et al. 2008,
324 Sanders et al. 2008, and Cea and Vázquez-Cendón 2010). All unknown variables were defined
325 at the center of each cell. To ensure numerical stability in the basic equations, a flux difference
326 scheme (FDS) was adopted for the advection and source terms. A slip-wall condition was
327 specified at the channel wall. At the upstream boundary, an inflow discharge hydrograph was
328 applied as a boundary condition. Water depth at the downstream end of the domain was also
329 specified as the boundary condition. Flow through the ballast layer was evaluated by applying
330 the following parameters:

331 $$\phi=0.47, a=0.79, b=25.1 \tag{13}$$

for the ballast area based on Table 1 and Eqn. 2 and

$$\phi = 1,\ a = 0,\ b = 0 \tag{14}$$

for the open-water area, where bed friction is the only source of energy loss. Note that U in Eqns. 2 and 3 represents the bulk velocity and $U = \phi\sqrt{u^2 + v^2}$. The model parameters used here were determined based on the experimental results of q = 0.0015 m^2/s ~ 0.018 m^2/s; agreement was confirmed for the entire range. The Manning coefficient, n, was set to 0.01 m$^{-1/3}$ s in order to represent the smooth surface of the experimental channel.

3.2 Model validation

Water surface profiles evaluated using the numerical model for the upstream boundary conditions of q = 0.016 m^2/s and q = 0.034 m^2/s were compared to the corresponding experimental profiles in Figure 12. In the simulation, the critical water depth corresponding to the inflow discharge was used as the downstream boundary condition. In both inflow conditions, adequate agreement between the calculated and measured water surface profiles at the center and downstream end of the ballast layer was confirmed. Ballast breaching occurs at the downstream end of the embankment, so the flow representation in this area is critical for evaluating the breaching process. For the condition of q = 0.016 m^2/s (labeled as QS in figure), the water surface in the ballast layer was located under the top of the ballast layer and did not reach the bottom of the sleepers. The water profile estimated by the flow model reasonably represented the experimental values (the filled-in open diamond symbols with error bars in Figure 12), especially for the fine calculation grid results. For the condition of q = 0.034 m^2/s in the experiment, the upstream end of the ballast layer was fully submerged but extensive ballast breaching was not initiated.

In the simulation, the ballast layer was considered to be infinitely high, and the slopes of the upstream and downstream ends were omitted and modeled as a vertical wall, as shown by the vertical hatched area in Figure 12. These simplifications were required so we could adopt a shallow-water approximation in order to model the flow. The water stage in the upstream area (the open squares in Figure 12), in which an open-water surface was formed above the ballast layer in the experiment, was overestimated in the simulation result because open-water flow experiences less flow resistance as compared to resistance of flow through the ballast layer. The water profile in the downstream subsurface flow area (the filled square in Figure 12) was reasonably represented in the simulation but was overestimated by approximately 20%. This overestimation is expected to be related to the three-dimensional flow features of outflow areas of the ballast region. These factors cannot be considered in the framework of the numerical model used here.

To estimate the local critical condition for the onset of ballast breaching, flow through a ballast layer was calculated for the condition of q = 0.040 m^2/s. For this condition, breaching in Case A was initiated in the experiment. The bulk velocity, U, at the downstream end of the ballast layer that was estimated by the numerical model was approximately U = 0.20 m/s (or the seepage velocity of $u=U/\phi$=0.43 m/s). The force acting on the ballast layer is evaluated in Eqn. 12, where τ_{px} and τ_{py} correspond to the forces acting on the ballast per unit area and are correlated with the local velocity components. The energy slope for ballast seepage under the condition of U = 0.20 m/s is I_e = 1.2.

The stability condition of a single grain on a rough bed in turbulent flow can be estimated as (Iwagaki 1956, Dey 1999):

$$\left[F_G - F_L\right]\tan\varphi = F_D \tag{15}$$

where F_G is the gravitational force and is estimated as $F_G = (\rho_s - \rho)g\frac{\pi}{6}d^3$; ρ_s is the mass density of sediment; d is the sediment diameter; F_L is the lift force; φ is the frictional angle; and F_D is the drag force. The left hand term of Eqn. 15 accounts for fictional force and is used to keep the position and the right hand term corresponding to the fluid force. The contribution of the lift force due to turbulence has been reported to be relatively minor (Iwagaki 1956), so the left hand term of Eqn. 15 can be assumed to be independent of the flow condition. By using the energy slope concept (Eqns. 1 to 3), the drag force can be accounted for by:

$$F_D = -\frac{\partial p}{\partial x}d\frac{\pi}{4}d^2 = \rho g I_e d\frac{\pi}{4}d^2 . \tag{16}$$

Accordingly, the energy slope, I_e, is a representative parameter for the critical condition and $I_e \approx$ 1.1 by assuming tan $\phi \approx 1$ (Iwagaki 1956). Therefore, the critical condition parameterized above, I_e =1.2, agreed well with this stability analysis.

3.3 The railway embankment breaching process

3.3.1 The ballast breach model

Considering the shape of the base soil embankment, flow through the railway embankment was numerically investigated. Figure 13 provides the simulated domain. The span-wise length of the domain (y direction) was 6 m. The longitudinal ends were treated as slip walls. A time-dependent flow rate was used as the inflow boundary condition and the water level was used as the downstream boundary condition. The elevation of the base embankment top was 1.0 m. The base embankment was represented by the rise of the impermeable bed and infiltration flow in the base embankment was neglected. Triangles with a side length of approximately 0.1 m were used to discretize the domain. This grid size was determined based on a tradeoff between accuracy and calculation time. To model the grass/plant-covered base embankment, the

401 Manning coefficient, n, was set to 0.03 $m^{-1/3}$ s at the base embankment surface. Both energy loss
402 and Manning friction loss were considered in the ballast layer area. During the flow simulation,
403 ballast calculation cells were replaced with open-water cells if the local velocity surpassed a
404 critical bulk velocity of U_c = 0.2 m/s.
405 During the process of ballast cell replacement with open-water cells, local water depth was
406 proportionally decreased to porosity in order to guarantee water volume conservation (Figures
407 14a and b). This sudden reduction in water depth caused an instantaneous and large water
408 surface gradient surrounding the newly replaced open-water area that accelerated water near the
409 newly replaced open-water cell. The accelerated water caused the neighboring cells to be
410 breached in the subsequent calculation time step; and this breaching front propagated upstream
411 for each time step until all of the ballasts were breached. To prevent this unrealistic sudden
412 breach propagation and to represent the gradual breaching process observed in the experiment, a
413 breaching speed limiter was introduced (Figure 14c). The ballast cell was switched, at 1.0 s
414 intervals, to an open-water cell using only the area located next to the open-water area. The
415 representative grid size was 0.1 m; thus, replacement of the grid at 1.0 s intervals corresponds to
416 a maximum breach propagation speed of 0.1 m/s.
417 Figure 15 compares time series for the breached ballast area that were calculated using
418 different breach propagation limiter values and indicates that the ballast breaching process is
419 almost insensitive to the propagation limiter when it is less than 0.2 m/s. The propagation
420 limiter was introduced in order to prevent unphysical breaching, but may be related to the
421 transport velocity of breached ballast particles and a three-dimensional slope failure process at
422 the downstream end. In this simulation, the time duration of the ballast breach is regulated by
423 the propagation limiter. Therefore, railway breaches caused by high wave overtopping, such as
424 that from a tsunami, are not assured by the ballast breach model introduced here. We focused on
425 the process that occurs under conditions of a gradual rising of the water level during fluvial
426 flooding, where the time duration of breaching is regulated by how quickly the water level rises.
427 In the breaching simulation framework employed in this paper, the transport process for
428 ballast particles eroded from the embankment was neglected and was treated as if particles
429 instantly disappeared from the domain. Flow at the downstream side of the embankment top
430 was shallow but fast, and the flow was almost critical ($Fr \approx 1$). Flow observed in this area during
431 the experiment was highly turbulent. These flow conditions caused eroded ballast particles to
432 immediately transport downstream. Therefore, eroded ballast particles have a limited impact on
433 the upstream ballast breaching process for the case of gradual breaching that occurs during
434 fluvial flooding.
435
436 *3.3.2 Heterogeneous breaching*

437 The trial calculation conducted in the preceding sub-section revealed that the perfectly
438 homogeneous embankment caused uniform flow in the span-wise direction (y-axis) and resulted
439 in uniform ballast breaching. In reality, flow through the ballast will not be completely uniform
440 due to the effects of the upper structure (rails and sleepers) and the heterogeneity of the ballast
441 material. Therefore, uniform breaching will not occur in an actual breach. To avoid this
442 unrealistic phenomenon and to account for heterogeneity in a physical railway embankment in
443 the simulation, small two-dimensional notches (approximately 0.15 m) were designed at the
444 downstream end of the ballast within the calculation grid. For this embankment, the calculation
445 began with a steady flow under the small inflow boundary condition (q = 0.03 m^2/s). The inflow
446 discharge hydrograph is depicted in Figure 16. The inflow rate was subsequently increased from
447 q = 0.03 m^2/s to q = 0.08 m^2/s over 2,000 s. A small water depth, 0.03 m, was applied as the
448 downstream boundary condition. The slope of the base embankment ($0 < x < 1.6$) was quite
449 steep (1:1.6) and supercritical flow was formed here so that flow on the embankment was
450 insensitive to the downstream boundary condition, with the exception of a high downstream
451 water level.
452 Figure 16 also provides the temporal change in the water stage at the upstream reservoir
453 point (located at x = -7.0, y = 0.0 m). Bed elevation at the gauging point was 0 m. Thus, the
454 water stage and the water depth were identical. Here, the water stage was increased almost
455 linearly with the flow rate increment. Ballast breaching began at t = 200 s and the upstream
456 water depth was approximately h = 1.7 m. After t = 1,560 s, the water stage began to rapidly
457 decrease. The flow rate at the peak water stage was q = 0.08 m^2/s. This value was approximately
458 twice the critical flow rate required to initiate ballast breaching in Case A (no upper structure: q
459 = 0.04 m^2/s, as shown in Figure 9). The water stage was reduced to h = 1.4 m from a peak value
460 of h = 2.0 m. This sharp decrease in the upstream water stage was due to the sudden reduction in
461 total energy loss as a consequence of ballast breach penetration.
462 Figure 17 displays snapshots of the flow at the initial stage of breaching (t = 0 s), during
463 breaching (t = 1,200 s), and at breach penetration (t = 1,560 s and t = 1,620 s). Due to space
464 limitations, the three left-hand side columns depict the downstream portion of the simulation
465 domain. The right-hand column (t = 1,620 s) depicts the entire simulation domain.
466 In the top row in Figure 17, enlargement of the open-water cell (indicated in light gray)
467 begins at the downstream end where small notches were intentionally made to introduce
468 heterogeneity. The ballast breach propagated to the upstream end and a tree-network pattern
469 developed upstream. The total length of the downstream boundary of the ballast layer increased
470 as a consequence of the breach. Development of a heterogeneous breached area was observed at
471 the actual damage sites (refer to Figures 1b, c, and d). The spatial structures and development
472 process exhibited similarities with the formation of amphitheater-headed valleys by

473 groundwater seepage in sapping processes (Laity and Malin 1985, Marra et al. 2014), whereas
474 the space and time scales of the processes differed.
475 Flow resistance in the open-water area was low as compared to flow resistance within the
476 ballast. Thus, water flow in the ballast area converged to the newly breached area. The flow
477 convergence effect can be confirmed in the second row in Figure 17. Here, the flow-field is
478 visualized using the line-integral convolution (LIC) method (Cabral and Leedom, 1993), a
479 texture-based flow visualization method, and has the advantage of illustrating detailed and
480 complex flow field features. Direction of the texture corresponds to the local flow direction. The
481 color of the texture correlates to the flow rate per unit width, hU. The flow direction in the
482 ballast layer was significantly affected by breaching. As the area changed from a ballast cell to
483 an open-water cell, a large unit discharge (indicated with orange and red) was observed.
484 Approaching flow in the ballast area converged to the breached area and the stream-line was
485 curved. The flow rate of the effluent from the area that was not breached at the downstream end
486 of the ballast was small. These flow patterns can also explain the amphitheater-headed valley
487 formation process in the ballast material (Laity and Malin 1985, Marra et al. 2014).
488 Prior to the breach penetrating the upstream end, flow in the upstream reservoir was
489 almost parallel and uniform. Following breach penetration (t = 1,620 s), flow in the upstream
490 reservoir suddenly changed from the previously uniform and parallel flow pattern to a sink flow
491 pattern (two right sub-figures in the second row in Figure 17). After breach penetration, almost
492 all of the water mass flowed through the breached open-water passage. Total head loss between
493 the upstream and downstream areas was drastically reduced following breach penetration and
494 caused a sudden reduction in the upstream water stage after t = 1,680 s, as shown in Figure 16.
495 As shown in the Froude number distribution depicted in the third row in Figure 17, flow on top
496 of the base embankment was a mixture of subcritical and supercritical flows, whereas flow on
497 the down-slope was always supercritical. The area downstream of the breach finger exhibited a
498 supercritical jet flow that formed behind the breached area. The result implies that breached
499 ballast particles do not influence the upstream flow. The flow concentration in the breaching
500 path influenced flow downslope of the embankment and may have caused base soil
501 embankment erosion.
502 The shear velocity distribution depicted in the bottom row in Figure 17 indicates that an
503 almost constant and relatively small shear velocity was observed in the initial phase (t = 0 s).
504 After propagation of the breach, a large local shear velocity (approximately 0.6 m/s) was
505 observed downstream of the main breach finger (right 1st subfigure in Figure 17). The largest
506 shear velocity was observed following breach penetration.
507
508 *3.3.3 Discussion: What will occur following breach penetration?*

509 The upstream water depth at the moment of breach penetration was estimated to be
510 approximately 2 m (1 m above the top of the base embankment in the simulation). By adopting
511 the broad-crested weir concept, the instantaneous and maximum discharge per unit width after
512 ballast breaching penetration can be estimated as 2.67 to 3.05 m^2/s based on the broad-crested
513 weir equation:
514 $$q = \alpha H^{3/2} \quad (17)$$
515 where α is a coefficient that depends on the geometry of the weir and that has a value that
516 ranges from 2.67 to 3.05; and H is the water elevation from the weir top (Chow, 1959). The
517 flow rate q = 2.67 to 3.05 m^2/s is two orders of magnitude larger than the flow rate required to
518 initiate the ballast breach (q = 0.04 m^2/s) and breach penetration (q = 0.08 m^2/s). This large
519 overtopping flow rate may cause erosion of the base embankment.
520 For a case in which the upstream impoundment has a small capacity, the upstream water
521 stage will rapidly decrease following ballast breaching. Conversely, if the upstream
522 impoundment is sufficiently large, the upstream water stage will remain constant for a long
523 period of time. If the water stage at the upstream impoundment is conserved following base
524 embankment breaching (not ballast layer breaching), temporal overflow discharge may increase
525 due to the increment of the overtopping water depth, H, in Eqn. 17.
526 Our analysis in this section was based on the properties of a new ballast material. For a case
527 in which an embankment is composed of the used material, the critical water depth required to
528 begin extensive breaching and to complete penetration of the ballast breach may differ from the
529 critical depths evaluated due to differences in the physical and dynamic properties of the
530 respective materials. The maximum and instantaneous flow rate for complete penetration of the
531 ballast may also be different for the used material case because of the differences in both energy
532 loss in the porous flow and the critical flow condition required to start a breach.
533
534 **4. Conclusions**
535 In this study, the process of railway embankment breaching caused by ballast layer breach
536 was experimentally and numerically investigated. First, ballast material properties, including
537 flow resistance, were specified. A full-scale ballast layer, including full-scale rails and sleepers,
538 was installed within a 1-m-wide open channel, and flow through the ballast layer and the
539 breaching process were investigated. The critical flow rate per unit width was 0.045 m^2/s and
540 the upstream water depth was 0.67 m from the bottom of the ballast layer within the upper
541 structures. Second, a two-dimensional flow model accounting for energy loss through the ballast
542 layer was developed.
543 For our simulation, a simplified ballast breaching model was implemented. The water flow
544 profile, estimated using the numerical model, was validated based on a comparison of

545 experimental results and reasonable agreement was observed. Flow through the railway
546 embankment, including the base embankment, was numerically analyzed. The development of
547 breaching was initiated with a small flow rate (approximately q = 0.04 m^2/s), and the breaching
548 area displayed a non-uniform and periodic pattern that was also found in field observations (e.g.,
549 Figure 1). The process is similar to amphitheater-headed valley formation, and water flow in the
550 ballast area converged to the breached open-water course. When the breached open-water
551 course reached the upstream end of the ballast, an open-water course that directly connected the
552 upstream impound with the downstream embankment slope emerged. Subsequently, upstream
553 reservoir water flow converged to the breached open-water pathway. This flow convergence
554 caused a local flow concentration. As a result, a large shear velocity was observed behind the
555 breached area, suggesting that the risk of base embankment erosion is impacted and enhanced
556 by ballast layer breaching.
557 We also introduced a simple breach model in order to represent ballast breaching
558 propagation under flow conditions that could not be tested in our experiment. The critical water
559 level from the upstream impound to breaching penetration was estimated as 1.0 m above the top
560 of the base embankment (0.5 m above the top of the ballast layer), and the probable unit flow
561 rate was estimated to range from 2.67 to 3.05 m^2/s. The results obtained and discussed in the
562 paper are invaluable for analyzing the failure risk of railway embankments in flood plains.
563 An additional breaching experiment will be required in the future in order to
564 validate/improve the numerical model and to verify the critical conditions for ballast breaching
565 penetration. The effects of gravel compaction and the clogging of fine sediments in the pore
566 space between the ballast should be evaluated in order to obtain more reasonable flow
567 conditions to account for the failure risk of the railway in use. The critical flow condition for the
568 breaching of base soil embankments covered with vegetation must also be evaluated in order to
569 understand the complete process of railway embankment breaching. The ballast breach model is
570 based on daring assumptions such as the shallow-water approximation and the propagation
571 limiter. To understand the breaching process in greater detail, more physically based and
572 detailed numerical modeling should be utilized.
573
574 **Acknowledgements**
575 Our study was partially funded by grants from the Chugoku Civil Engineering Foundation for
576 Mutual Aid, Japan, and the Foundation for River and Watershed Environment Management,
577 Japan. We appreciate Dr. Ichiro Ario at Hiroshima University for his useful suggestions at the
578 beginning of the study. Susumu Yoshida at the West Japan Railway Company provided
579 information regarding maintenance of the railway that was essential for conducting this study.

We are also grateful to Kenji Futatsugi for providing photos of Yamaguchi railway failures that occurred during 2010.

References

Arbhabhirama, A. and Dinoy, A., 1973, Friction factor and Reynolds number in porous media flow, J. Hyd. Div., Proc. ASCE, 99 (HY6), 901-911.

ASCE/EWRI task committee on dam/levee breaching, 2011, Earthen Embankment Breaching, Journal of Hydraulic Engineering, 1548-1564.

Cabral, B. and Leedom, L., 1993, Imaging vector fields using line integral convolution, Proc. 20th annual conf. on Computer graphics and interactive techniques SIGGRAPH 93.

Cea, L. and Vázquez-Cendón, M.E., 2010, Unstructured finite volume discretization of two-dimensional depth-average shallow water equations with porosity, International Journal for Numerical Methods in Fluids, 63, 903-930.

Costa, J.E., 1985, Floods from dam failures, Open-File Rep. No. 85-560, USGS, Denver, 54.

Chow, V.T., 1959, Open-channel hydraulics, McGraw Hill, reprinted by Blackburn press.

Dey, S., 1999, Sediment threshold, Applied Mathematical Modelling, 23, 399-417.

Fujita, I., Ito, T. and Sayama, T., 2012, Inundation Analysis of 2009 Chikusa River Flood and Comparison of Evacuation Criteria, Journal of Flood Risk Management, DOI: 10.1111/jfr3.12020.

Guinot, V. and Soares-Frazão, S., 2006, Flux and source term discretization in two-dimensional shallow water models with porosity on unstructured grids, International Journal for Numerical Methods in Fluids, 50, 309-345.

Gyasi-Agyei, Y., Sibley, J., Ashwath, N., 2001, Quantitative evaluation of strategies for erosion control on a railway embankment batter, Hydrological Processes, 15, 3249-3268.

Hassanizadeh, S.M. and Gray, W.G., 1987, High velocity flow in porous media, Transport in porous media, 2, 521-521.

607 Iwagaki, Y., 1965, Fundamental study on critical tractive force, Trans. JSCE, 41, 1-21.
608 Japan Railway Civil Engineering Association, 2000-2011, The Journal of Japan Civil
609 Engineering Association, May issue for each years.
610 Laity, J. E. and Malin, M. C., 1985, Sapping processes and the development of theater-headed
611 valley networks on the Colorado Plateau, Geological Society of America Bulletin, 96, 2,
612 203-217.
613 Marra, W. A., Braat, L., Baar, A. W. and Kleinhans, M. G., 2014, Valley formation by
614 groundwater seepage, pressurized groundwater outbursts an crater-lake overflow in flume
615 experiments with implications for Mars, Icarus, 232, 97-117.
616 Masuoka, T. and Takatsu, Y., 1996, Turbulence model for flow through porous media, Int. J.
617 Heat Mass Transfer, 39(13), 2803-2809.
618 Michioku, K., Maeno, S., Furusawa, T. and Haneda, M., 2005, Discharge through a permeable
619 rubble mound weir, Journal of Hydraulic Engineering, 131, 1, 1-10.
620 http://dx.doi.org/10.1061/(ASCE)0733-9429(2005)131:1(1)
621 Ministry of railways, 2005, Guidelines on temporary and permanent restoration of embankment
622 after breach/washouts, Government of India, Report No. Ge: G-7.
623 Kaneko, Y., 2010, The damages to the railway of the Kishin line between Kyutoku station to
624 Mimasakadoi station due to the typhoon Etau, J. of Japan Rail Way Civil Eng. Association, 6,
625 450-451. (in Japanese)
626 Polemio, M. and Lollino, P., 2011, Failure of infrastructure embankments induced by flooding
627 and seepage: a neglected source of hazard, Natural Hazards and Earth System Sciences, 11,
628 3383-3396.
629 Railway Technical Research Institute, 2007, Standards for railway infrastructure, earthen
630 structures, Maruzen Co. Ltd., in Japanese.

631 Sanders, B.F., Schubert, J.E. and Gallegos, H.A., 2008, Integral formulation of shallow-water
632 equations with anisotropic porosity for urban flood modeling, Journal of Hydrology, 362,
633 19-38. doi:10.1016/j.jhydrol.2008.08.009
634 Shigeda, M, Akiyama, J, Ura, M, Jha, AK, and Arita, Y., 2002, Numerical simulations of flood
635 propagation in a flood plain with structures, Journal of Hydroscience and Hydraulic
636 Engineering 20(2): 117–129.
637 Shige-eda, M. and Akiyama, J. 2003, Numerical and experimental study on 2D flood flows with
638 and without structures, Journal of Hydraulic Engineering, 129(10), 817–821.
639 Shimizu, Y., 1992, Study on open channel flow on various roughness beds, Doctoral
640 dissertation, Kyoto University, Japan, in Japanese.
641 Soares-Frazão, S., Lhomme, J., Guinot, V. and Zech, Y., 2008, Two-dimensional shallow-water
642 model with porosity for urban flood modelling, Journal of Hydraulic Research, 46, 1, 45-64.
643 Trussell, R.R. and Chang, M., 1999, Review of flow through porous media as applied to head
644 loss in water filters, Journal of Environmental Engineering, 125 (11), 998-1006.
645 Tsubaki, R., Nakayama, Y. and Fujita, I., 2008, The design secret of kyokusui-no-en's
646 meandering channel, Journal of Visualization, 11(3), 265-272.
647 Tsubaki, R, and Fujita, I. 2010. Unstructured grid generation using LiDAR data for urban flood
648 modelling, Hydrological Processes, 24(11): 1404-1420.
649 Tsubaki, R., Kawahara, Y., Fujita, I. and Sayama, T., 2011a, Analysis of Railway Embankment
650 Breach Due to Typhoon-induced Flooding, 34th IAHR Congress, on CD-ROM, Brisbane,
651 Australia, July.
652 Tsubaki, R., Fujita, I. and Tsutsumi, S., 2011b, Measurement of the flood discharge of a
653 small-sized river using an existing digital video recording system, Journal of
654 Hydro-Environment Research, 5(4), 313-321.

655 Tsubaki, R., Kawahara, Y., Sayama, T. and Fujita, I., 2012, Analysis of geomorphic and
656 hydraulic conditions causing railway embankment breach due to inundation caused by heavy
657 rainfall, Journal of Hydraulic and Hydroscience Engineering, JSCE, 30(1), 87-99,.
658

Figure captions

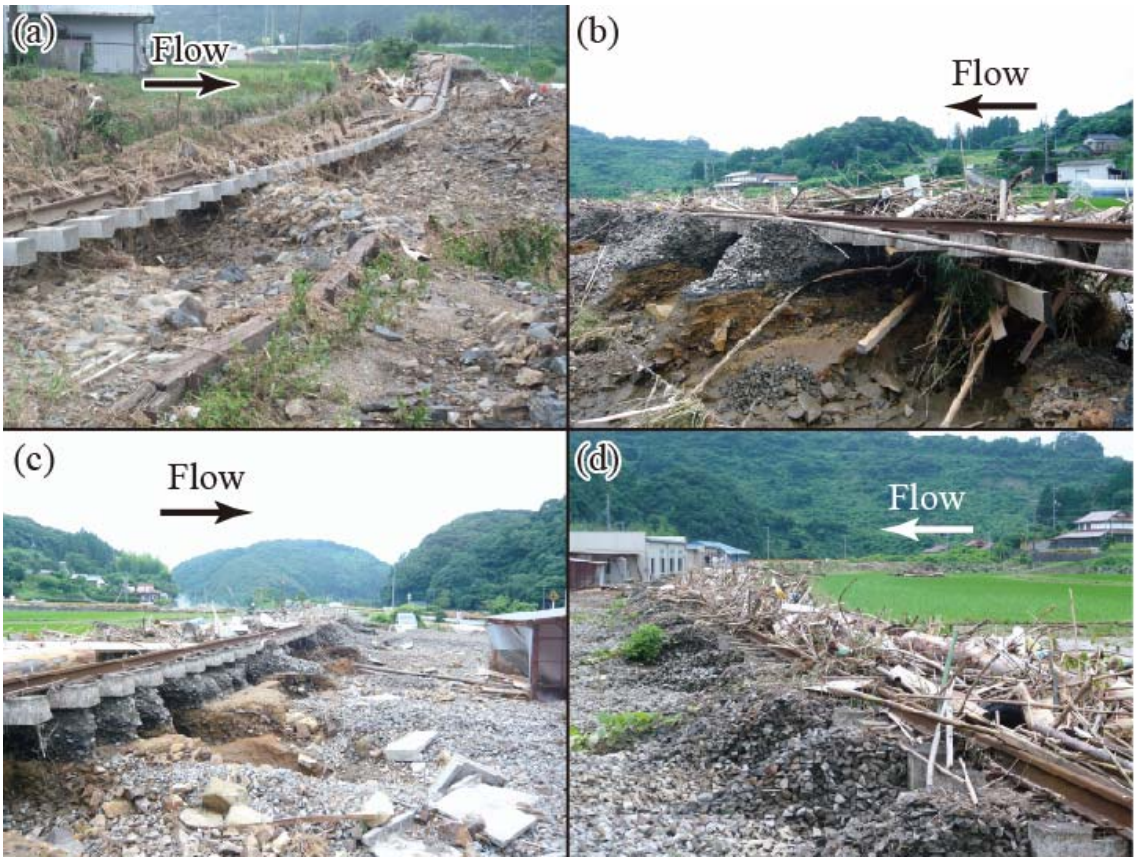

Figure 1 Breached railway embankments: (**a**) August 2009, Hyogo, Japan. (**b**) July 2010, Yamaguchi, Japan; close-up. (**c**) July 2010, Yamaguchi, Japan; from downstream to upstream. (**d**) July 2010, Yamaguchi, Japan; from upstream to downstream.

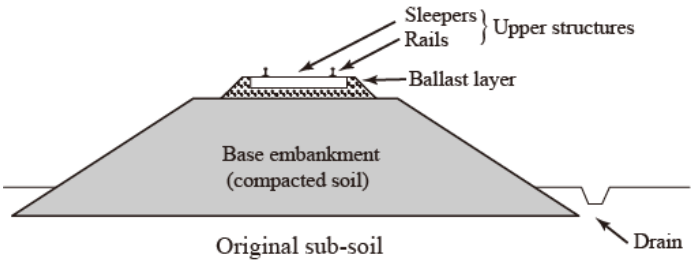

Figure 2 Schematic of a railway embankment for a non-electrified, single-track section.

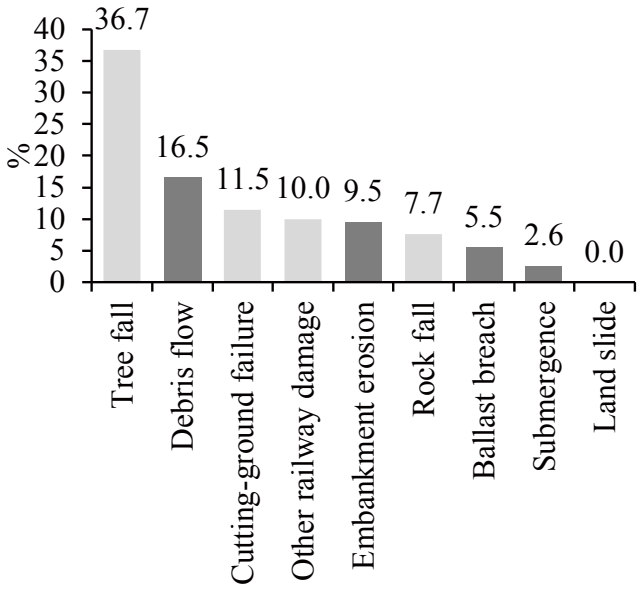

669

670 Figure 3 Percentage of natural hazards on railways from 1999 to 2010 as reported by the Japan
671 Railway Co., Ltd. and summarized by the Japan Railway Civil Engineering Association
672 2000-2011 (a total of 7,852 cases). Flow-related damage is represented by dark gray bars.
673

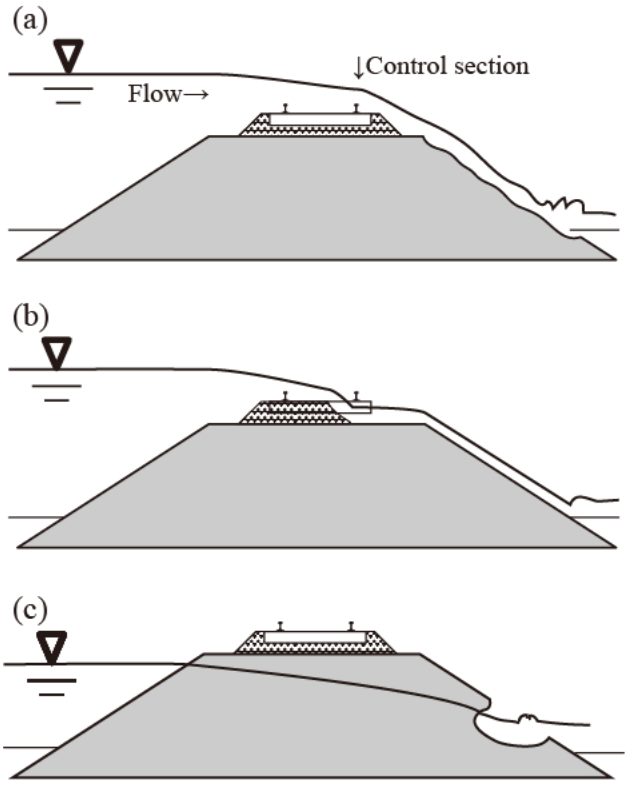

674

675 Figure 4 Possible types of railway embankment failures: (**a**) a lee slope breach; (**b**) a ballast
676 layer breach; (**c**) embankment seepage.

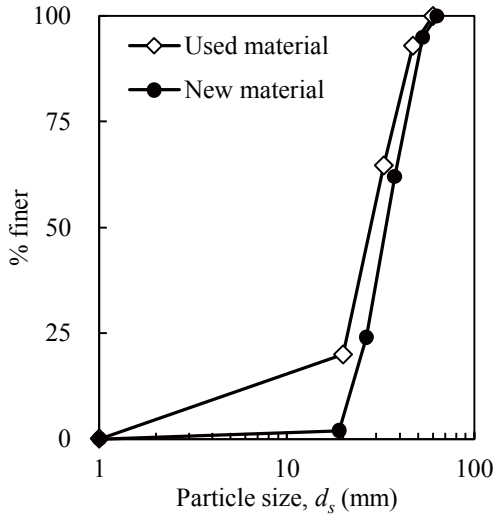

Figure 5 Particle-size distribution of new and used ballast materials.

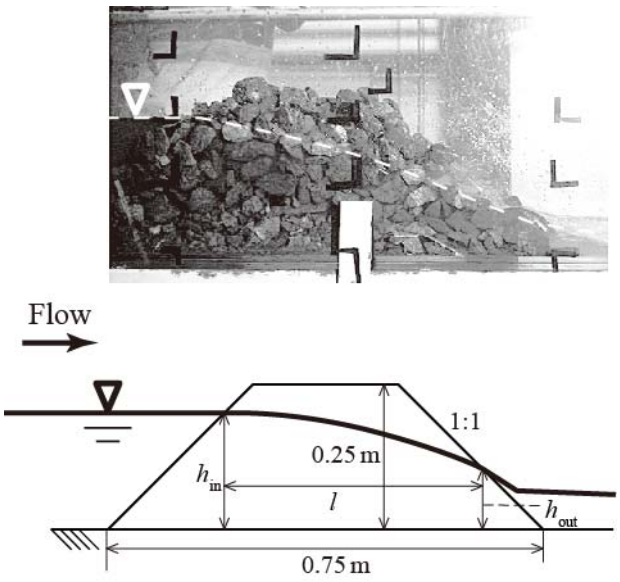

Figure 6 The experimental setup used to estimate energy losses.

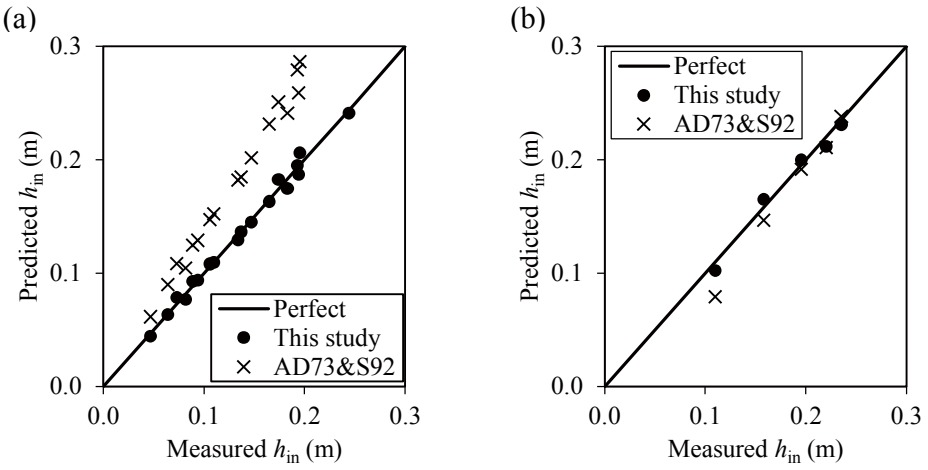

Figure 7 Validation of the estimation of energy losses: (**a**) new ballast material; (**b**) used ballast material. '*This study*' represents the upstream water depth modeled by Eqns. 2 and 3. '*AD73&S92*' provides results obtained using Eqns. 4 to 6 (Arbhabhirama and Dinoy 1973, Shimizu 1992) using corresponding material parameters as provided in Table 1.

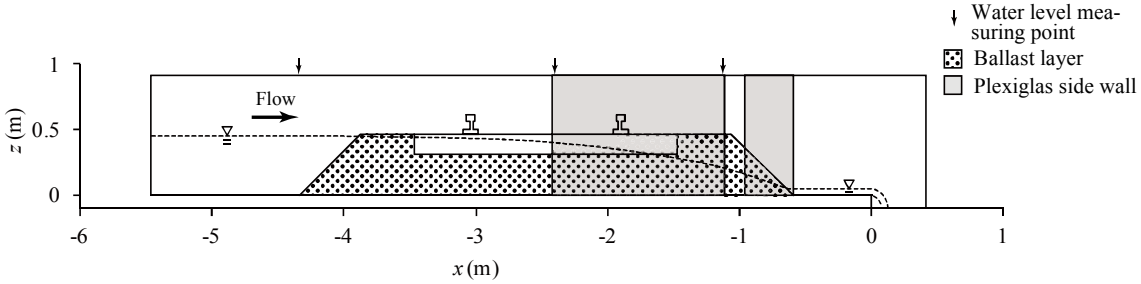

Figure 8 Configuration of the full-scale ballast layer experiment. The side wall of the *shaded area* was composed of Plexiglas to enable observation of the water profile.

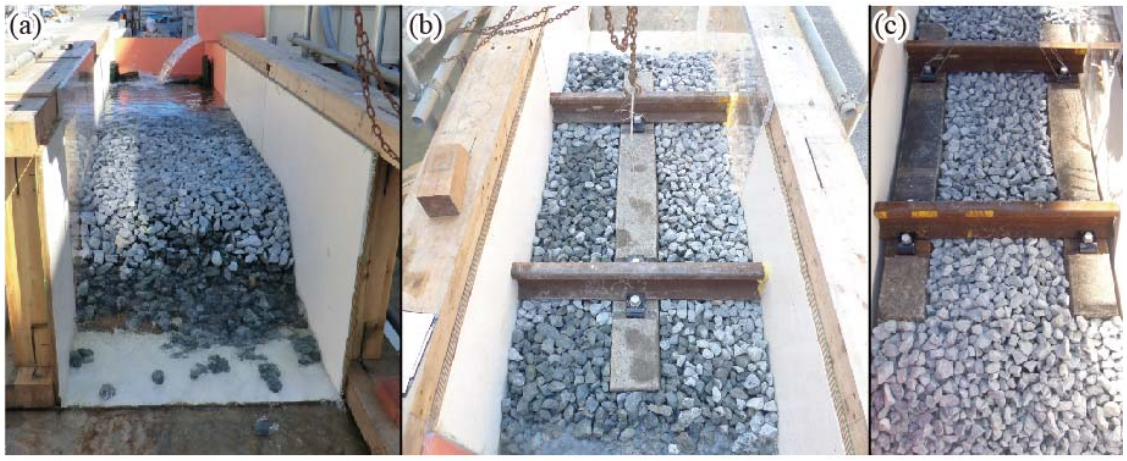

Figure 9 Full-scale ballast layer experiment: (**a**) Case A; (**b**) Case B; (**c**) Case C.

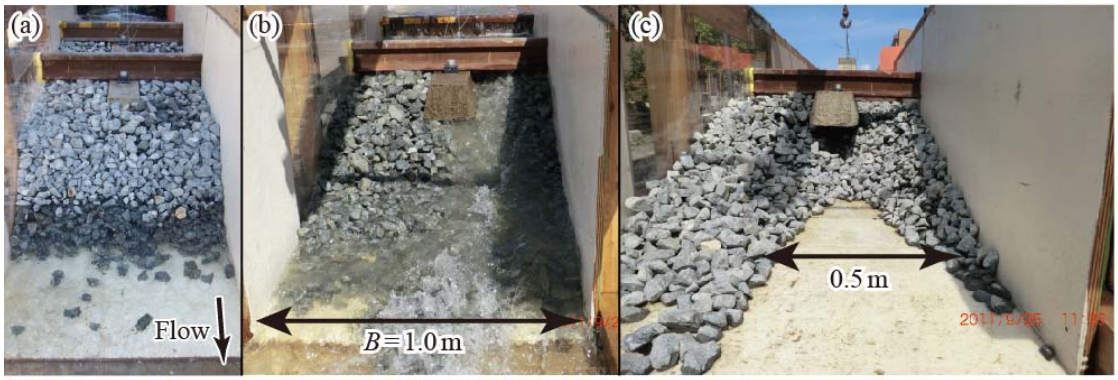

Figure 10 Sample of the breaching process for Case B: (**a**) initial breaching phase; (**b**) extensive breaching phase; (**c**) after flow terminated.

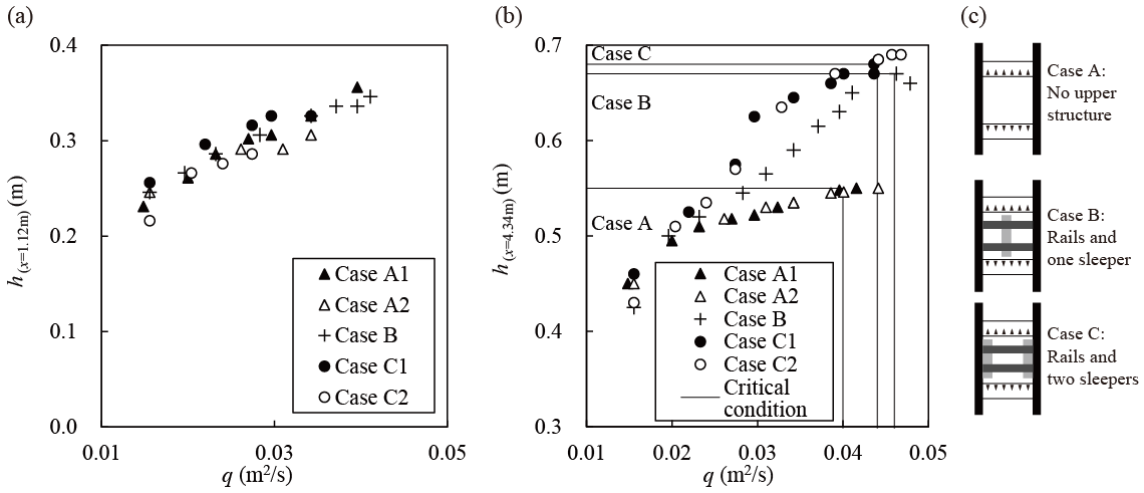

Figure 11 Relationship between flow rate per unit width and the water depth: (**a**) at the embankment downstream (x = -1.12 m); (**b**) at the upstream reservoir (x = -4.34 m); (**c**) summarized plan views for cases A, B, and C. The measuring point x is depicted in Figure 8. Experiments for Cases A and C were conducted twice. Case A1 and Case C1 indicate the first trial, and Case A2 and Case B2 indicate the second trial. For Case B, the experiment was performed once.

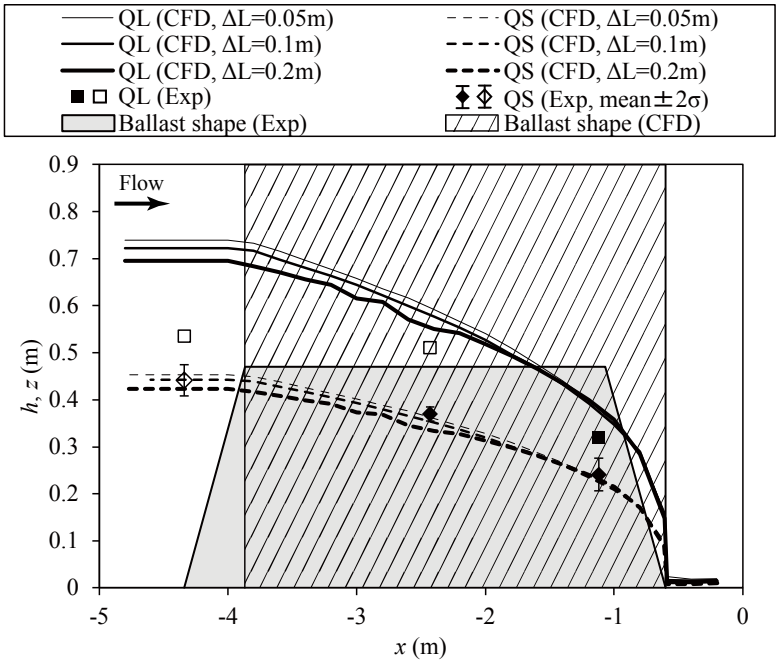

Figure 12 Water depth profiles of the experimental and calculated results for q = 0.016 m^2/s (labeled as *QS*) and q = 0.034 m^2/s (*QL*). *ΔL* indicates the representative grid size. The experimental result for q = 0.034 m^2/s was based on five trials. *Filled symbols* for the experimental result represent the sub-surface water level, whereas *open symbols* represent the open-surface water level.

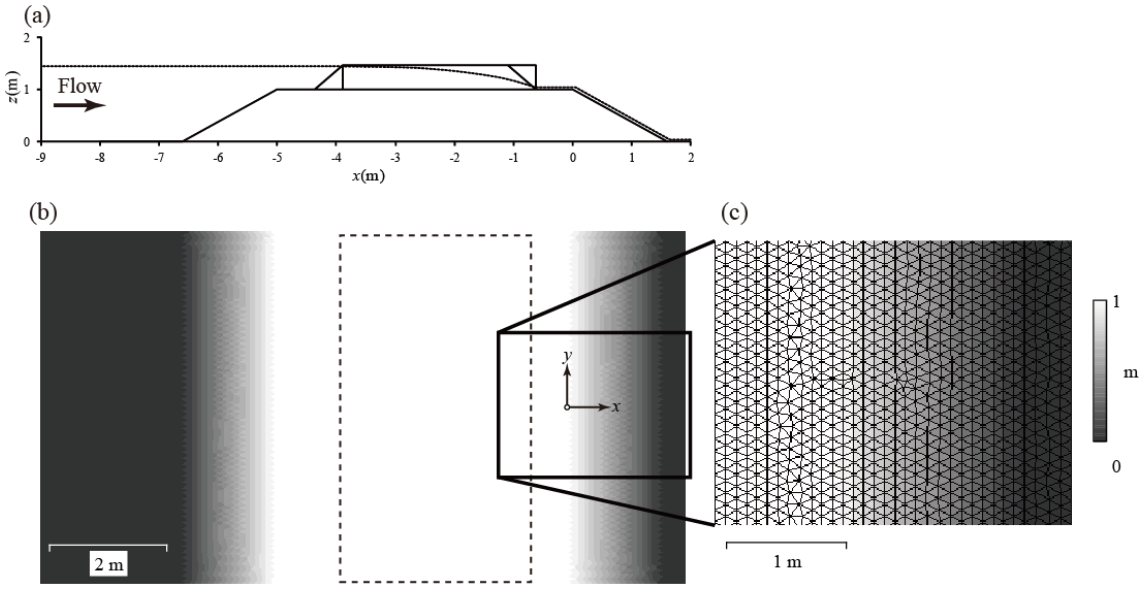

Figure 13 Configuration for the flow simulation on the full-scale railway embankment: (**a**) cross-section; (**b**) plan of calculation grid; (**c**) close-up of the calculation grid. *Gray tones* in subfigures (**b**) and (**c**) correspond to elevation of the soil embankment.

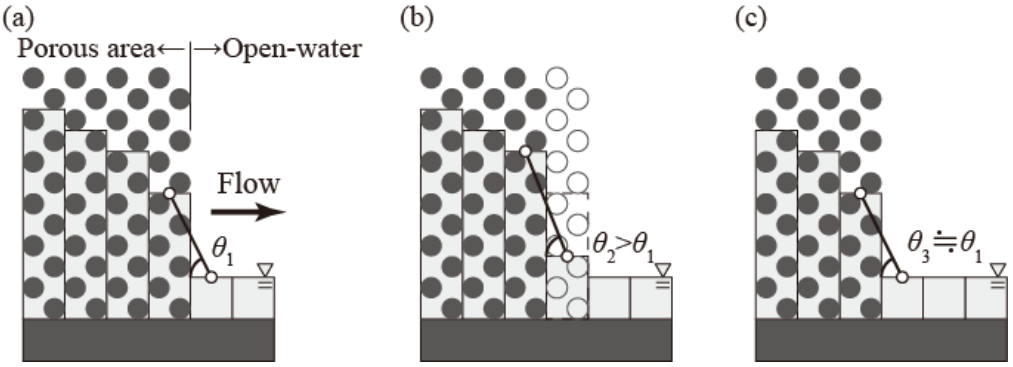

Figure 14 Steep water slope formation due to porous area breaching surrounding the porous area and open-water boundary: (**a**) before breaching when a steep water slope is formed at the boundary between porous and open-water areas; (**b**) just after breaching when the water slope becomes steeper because of a reduction in the water depth due to mass conservation as a consequence of the sudden change in porosity; (**c**) the water profile surrounding the porous and open-water boundary after reconstruction.

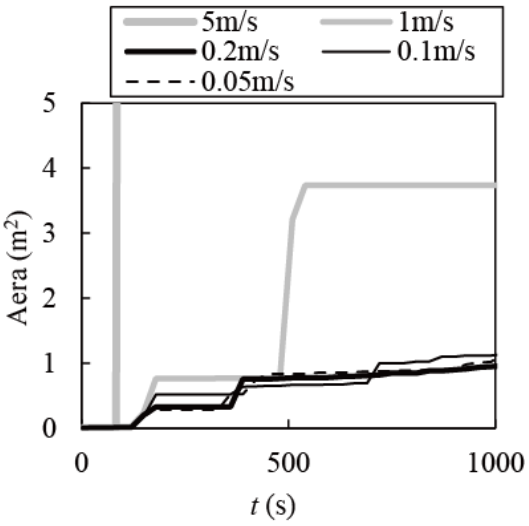

Figure 15 The sensitivity of the breach propagation velocity limiter to the breached area.

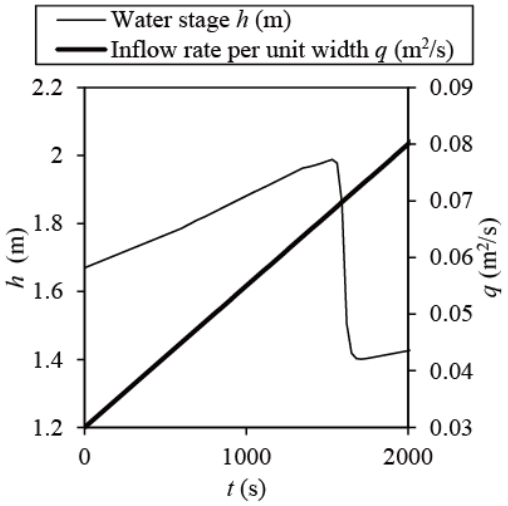

732

733 Figure 16 Hydrograph of the discharge (*thin line* and the right axis) and water stage (*thick line*
734 and the left axis).

735

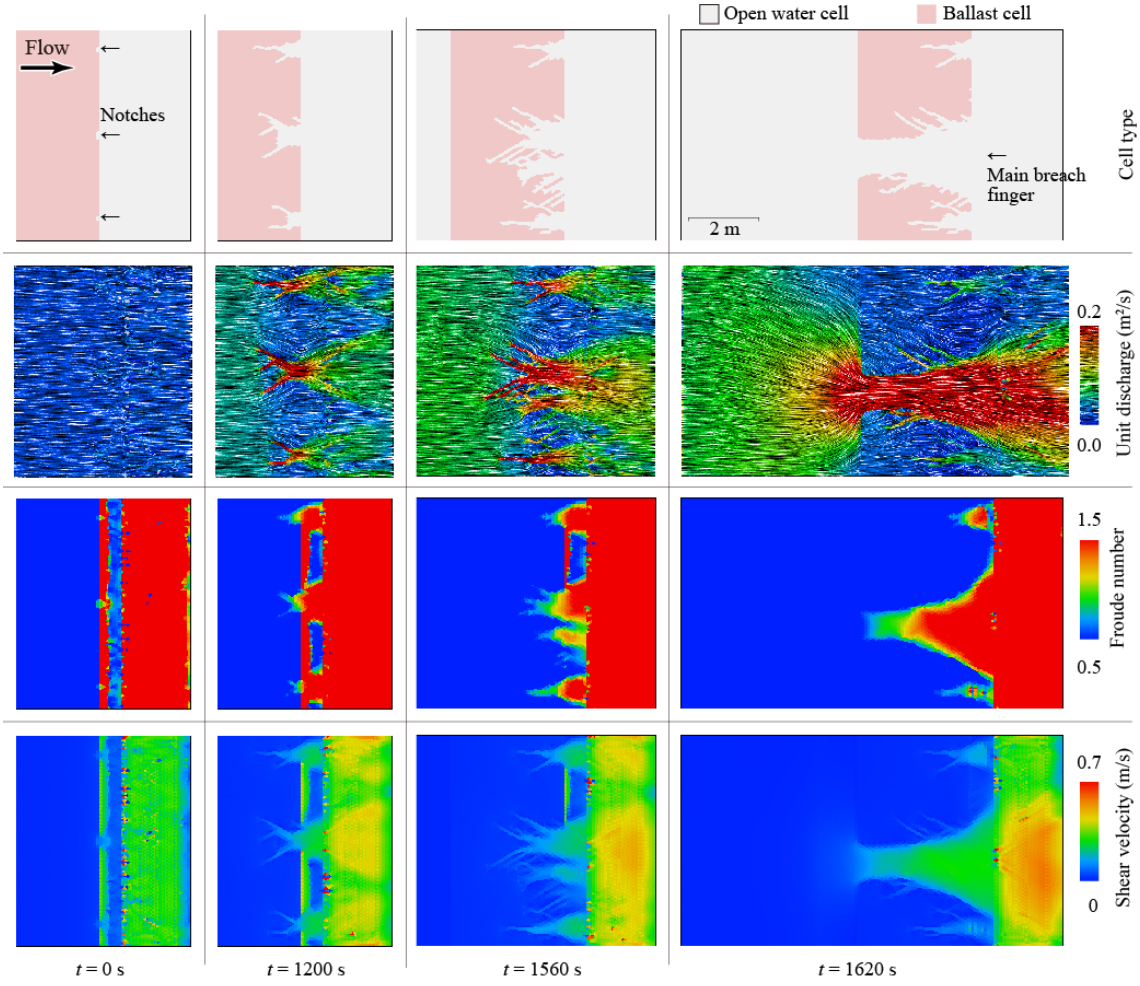

736

737 Figure 17 The propagation of a ballast breach. From left to right, four time points are shown (t =
738 0 s, 1,200 s, 2,600 s, and 2,780 s). From top to bottom: the cell types, the flow-field visualized
739 using LIC, the Froude number contour, and the bottom shear velocity.
740

741 **Table(s)**

742

743 **Table 1 Properties of the ballast materials.**

	Density (g/cm^3)	Porosity (-)	Diameter d_{50} (mm)	Sample from
New material	2.65	0.47	32	Hiroshima Prefecture
Used material	2.55	0.44	26	Hyogo Prefecture

744